This manuscript was accepted by Phys. Plasmas. Click here to see the version of record.

The Kelvin-Helmholtz instability of boundary-layer plasmas in the kinetic regime

Benedikt Steinbusch,[1, a] Paul Gibbon,[1, 2, b] and Richard D. Sydora[3, c]
[1] Institute for Advanced Simulation, Jülich Supercomputing Centre, Forschungszentrum Jülich GmbH, D–52425 Jülich, Germany
[2] Centre for Mathematical Plasma Astrophysics, Department of Mathematics, Katholieke Universiteit Leuven, Belgium
[3] Department of Physics, University of Alberta, Edmonton, Alberta T6G 2E1, Canada

(Dated: 13 May 2016)

The dynamics of the Kelvin-Helmholtz instability are investigated in the kinetic, high-frequency regime with a novel, two-dimensional, mesh-free tree code. In contrast to earlier studies which focused on specially prepared equilibrium configurations in order to compare with fluid theory, a more naturally occurring plasma-vacuum boundary layer is considered here with relevance to both space plasmas and linear plasma devices. Quantitative comparisons of the linear phase are made between the fluid and kinetic models. After establishing the validity of this technique via comparison to linear theory and conventional PIC simulation for classical benchmark problems, a quantitative analysis of the more complex magnetized plasma-vacuum layer is presented and discussed. It is found that in this scenario, the finite Larmor orbits of the ions result in significant departures from the effective shear velocity and width underlying the instability growth, leading to generally slower development and stronger nonlinear coupling between fast growing short-wavelength modes and longer wavelengths.

I. INTRODUCTION

The Kelvin-Helmholtz instability is an important and ubiquitous phenomena in magnetized plasmas. In principle it can occur in any situation where there are crossed, stationary magnetic and electric fields producing a sheared $\boldsymbol{E} \times \boldsymbol{B}$ drift, typically at plasma-vacuum boundaries where the differing gyro-radii of the ions and electrons generates a charge separation with associated electrostatic field. If the strength of the shear exceeds a certain threshold, Kelvin-Helmholtz (KH) vortices start to grow, feeding on the plasma kinetic drift energy. Like many instabilities it manifests itself in various guises depending on the time- and length scales dictated by the local plasma density, temperature and geometry. In space plasmas, the KH instability has long been touted as a likely candidate for coupling momentum and energy from the solar wind to and from the magnetosphere[1–3]. In laboratory magnetized plasmas, the KH instability is typically found in regions of tangency to walls or limiters, but can also form across separatrix layers or as a secondary instability in zonal flows developing from drift-wave-type turbulence. Experimental investigations of plasma structures and cross-field transport due to a competition between drift waves and sheared $\boldsymbol{E} \times \boldsymbol{B}$ rotation in linear plasma devices have been carried out in a number of plasma devices beginning with Q-machines[4]. In these linear devices the velocity shear is maximized in the shadow region of a limiter that is typically introduced in the plasma to restrict the plasma diameter and a great deal of progress has been made in characterizing shear flow instabilities in this region[5–7]. External generation and control of KH instabilities can be performed in these devices by externally biasing the plasma relative to the chamber walls[8].

A clear distinction can be made between the fluid regime, characterized by length scales L much larger than the ion gyro-radius $r_{\mathrm{L,i}}$ and correspondingly long timescales $t \gg \omega_{\mathrm{c,i}}^{-1}$; and the more complex, high-frequency kinetic regime, in which $r_{\mathrm{L,i}}/L \gg 1$. In the former instance the instability can be described by classic fluid theory[9] and has been successfully modeled with multi-dimensional MHD codes[10]. In this paper we focus entirely on the collisionless kinetic regime, revisiting a problem which was first tackled over 20 years ago by a series of papers utilizing particle-in-cell simulation to shed light on the long-lived vortex structures which develop after the initial linear growth phase.

One of the first works to consider this version of the KH instability was by Pritchett & Coroniti[11]. They considered a homogeneous plasma with an *initial velocity shear* $v_{0y}(x)$ and profile oriented perpendicular to the magnetic field $\boldsymbol{B}_0 = B_0\hat{\boldsymbol{z}}$, giving a self-consistent electrostatic field $E_{0x}(x) = -B_0 v_{0y}(x)$. This geometry is amenable to a full 2-fluid eigenmode analysis of the linear phase of the instability, allowing the authors to demonstrate agreement between the PIC simulations and the incompressible MHD equations in the small gyro-radius limit $r_{\mathrm{L,i}} \leq L$. In the opposite, kinetic case of interest they found that the linear growth rates were significantly reduced, and that the KH vortices grew and merged up to the largest wavelength permitted by the simulation box,

---

[a] b.steinbusch@fz-juelich.de
[b] p.gibbon@fz-juelich.de
[c] rsydora@ualberta.ca

ACCEPTED MANUSCRIPT

This manuscript was accepted by Phys. Plasmas. Click here to see the version of record.

ACCEPTED MANUSCRIPT

speculating that in reality, there should be physical limiting factors to the steady-state vortex size. Pritchett[12] followed up this work with a shorter study on a slightly different geometry in which the $\boldsymbol{E} \times \boldsymbol{B}$ drift and subsequent instability is driven by a localized electric field, pointing out that the KH mode in this configuration had growth rates vastly exceeding those for a similar ion-cyclotron instability[13].

A slightly different approach to the problem was taken by Horton et al.[14], who used an implicit, guiding center PIC code to study the KH instability for high magnetic field strengths and long time-scales. This choice allowed them to make quantitative comparison of the long-time vortex behavior with fluid theory. As in Ref.[11], their simulations were also set up with a homogeneous density and prescribed velocity shear profile with a characteristic width a of the form $v_y = v_0 \tanh(x/a)$, facilitating an extensive analysis of vortex dynamics and particle transport. They identified three stages of vortex development: i) exponential growth, ii) saturation of the fastest growing mode and subsequent merging, and iii) single vortex evolution. A complementary study in the same geometry was performed by Cai et al.[15], who compared the linear growth rates of the fluid ($r_{\mathrm{L,i}}/a \ll 1$) and kinetic ($r_{\mathrm{L,i}}/a > 1$) regimes over a wide range of parameters. Like Pritchett & Coroniti, Cai et al. used a 2D explicit PIC code, but with a special particle-loading algorithm to initialize the shear flow profile in equilibrium[16]. Despite the modest statistics, the 'quiet start' for the KH instability allowed them to observe up to 6 decades of exponential growth in some of the modes (see Fig.4 of Ref.[15], finding generally lower growth rates for larger Larmor radii.)

While the above works already shed light on the linear and nonlinear behavior of the kinetic KH instability, for ease of comparing with linear theory they all assumed a homogeneous plasma density. An attempt to model a true boundary layer more typical of plasma devices was made by Theilhaber & Birdsall[17–19], who considered a plasma in contact with a perfectly conducting wall (see Fig.1 of Ref.[18]). This scenario differs in a number of respects: first, the particle population is dynamic – particles being absorbed by the wall and re-injected pairwise within the plasma volume; second, the plasma-wall boundary layer and subsequent velocity shear are allowed to develop spontaneously via the charge separation resulting from the respective ion and electron gyro-radii. Interestingly, for the linear regime they also find agreement with fluid theory for long wavelength modes, but divergence at short wavelengths apparently due to finite-Larmor-radius (FLR) effects. A summary of these earlier works can be found in Table I.

The purpose of the present paper is to revisit the collisionless, kinetic KH instability problem in the context of a more general plasma-vacuum boundary layer, without imposing restrictions on the shear flow velocity or electric field. In doing so, we introduce a new, mesh-free technique based on an electrostatic tree code, using the linear growth regime to gauge its effectiveness against a traditional 2D PIC code in terms of performance and resolution of short-wavelength modes. An analogous comparison has recently been published by Umeda et al.[20], who benchmark a 2D2V Vlasov code against a PIC code in the low-frequency regime (neglecting the electron cyclotron motion). We also take advantage of the vastly improved computing power available since these early works, to probe the onset of the nonlinear phase of KH vortex dynamics with full electron and ion dynamics.

The paper is organized as follows: Section II describes the numerical model used to perform simulations of the various scenarios in the following sections. In Section III we benchmark the method by reproducing the dispersion relation of a warm magnetized plasma at homogeneous density and also comparing the results to a PIC simulation in equivalent geometry. This is followed in Section IV by a study of the classical Kelvin-Helmholtz instability in a homogeneous plasma. Then, we investigate a novel kind of instability at a free plasma-vacuum boundary layer in Section V identifying resemblances and departures from the classical case. The paper is concluded with a discussion in Section VI.

II. DESCRIPTION OF NUMERICAL MODELS

A. Tree Code

To treat the problem numerically, we model the plasma as an ensemble of particles confined to the x-y plane with no dependence on the z coordinate. The force between two particles (or strictly speaking, particle rods) i and j is thus:

$$\boldsymbol{F}_{ij} = \frac{q_i q_j}{2\pi \left\| \boldsymbol{x}_i - \boldsymbol{x}_j \right\|^2} \left(\boldsymbol{x}_i - \boldsymbol{x}_j \right). \tag{1}$$

Particle motion is governed by the Newtonian equations of motion with a force term that consists of a Lorentz force term due to the externally imposed magnetic field and the sum of all binary interactions with all other particles:

$$m_i \ddot{\boldsymbol{x}}_i = q_i \dot{\boldsymbol{x}}_i \times \boldsymbol{B}_0 + \sum_{j \neq i} \boldsymbol{F}_{ij} \tag{2}$$

The Barnes-Hut tree algorithm[21] lowers the complexity of evaluating the right hand side sum for every particle from $\mathcal{O}\left(N^2\right)$ to $\mathcal{O}\left(N \log N\right)$. It achieves this acceleration by replacing interactions between a particle and a compact group of multiple distant partners by a single interaction with the corresponding multipole moment. These moments are calculated explicitly for small groups or even single particles and are then combined into a hierarchy of coarser moments for increasingly larger groups in a tree data structure. An evaluation of the sum of pair

This manuscript was accepted by Phys. Plasmas. Click here to see the version of record.

TABLE I. Summary of previous studies of kinetic KH instability

Ref	$m_{\rm i}/m_{\rm e}$	$\omega_{\rm c,e}/\omega_{\rm p,e}$	$\omega_{\rm c,i}/\omega_{\rm p,i}$	$r_{\rm L,i}/\lambda_{\rm D,e}$	$r_{\rm L,i}/a$	Box size $L_x \times L_y$ ($\lambda^2_{\rm D,e}$)	Longest run
[11]	16-1836				0.19-1.5	128×128	$700\ \omega_{\rm p,e}^{-1}$
[12]	1836				0.032-2.4	128×64	$229\ \omega_{\rm c,i}^{-1}$
[14]	1600	10-80	0.006-0.03			$6.4\ a \times 6.4\ a$	$1000\ a/v_0$
[15]	16	0.1-0.5	0.006-0.03		0.1-1.0	128×512	$660\ \omega_{\rm p,e}^{-1}$
[17_19]	40	5.5	0.35-1.4		0.1-1.0	$5\ r_{\rm L,i} \times 40\ r_{\rm L,i}$	$437\ \omega_{\rm c,i}^{-1}$

interactions is equivalent to a traversal of the tree which selects as interaction partners those multipole moments that meet an acceptance criterion based on a target accuracy.

The force law given in equation (1) is the fundamental solution of the laws of electrostatics with open boundary conditions. To accommodate the periodic boundary conditions often used in simulations of plasma physics, the tree code regards the rectangular simulation domain as the unit cell of a periodic lattice and takes into account the contributions to the electric potential and field due to a large number of replicas of this unit cell along the lattice axes following a two-fold approach. The contribution due to the replicas in a thin layer around the central cell are calculated by explicitly shifting the x_i in equation (1) and running the same tree traversal algorithm as for the central cell. The thickness of the layer is chosen such that all replicas outside of it are well-separated from the central cell, i.e. their multipole expansion can be translated into a local Taylor-like expansion of the potential and the electric field that converges. Based only on the description of the periodic lattice, it is then possible to construct operators that efficiently calculate the contribution due to more than ten nonillion (10×10^{30}) periodic replicas[22,23]. Earlier incarnations of this code have been used in the context of ion acceleration from laser-plasmas[24]; a fully parallel version is described in[25].

We choose units that are based on collective quantities of the electron species in the unperturbed plasma: Length: electron Debye length $\lambda_{\rm D,e} = 1$; Time: inverse electron plasma frequency $\omega_{\rm p,e} = 1$; Mass: electron mass $m_{\rm e} = 1$; Charge: elementary charge $e = 1 = -q_{\rm e}$; Temperature: electron temperature $T_{\rm e} = 1$.

It immediately follows that $v_{\rm th,e} = \lambda_{\rm D,e}\omega_{\rm p,e} = 1$ and $\rho_{\rm e}/\epsilon_0 = -1$. The quantities describing electron cyclotron motion are in terms of the background magnetic field B_0: the cyclotron frequency $\omega_{\rm c,e} = B_0$ and the Larmor radius $r_{\rm L,e} = v_{\rm th,e}/\omega_{\rm c,e} = 1/B_0$. For the ion species, we define the mass $m_{\rm i} = \mu m_{\rm e}$, charge $q_{\rm i} = -q_{\rm e}$, and temperature $T_{\rm i} = \tau T_{\rm e}$, where μ is the ion/electron mass ratio; τ the temperature ratio. Thus, their characteristic length and time scales become $\lambda_{\rm D,i} = \sqrt{\tau}\lambda_{\rm D,e}$, $\omega_{\rm p,i} = \omega_{\rm p,e}/\sqrt{\mu}$, $r_{\rm L,i} = \sqrt{\mu\tau}r_{\rm L,e}$ and $\omega_{\rm c,i} = \omega_{\rm c,e}/\mu$. The units for the electric and magnetic field in this system are:

$$[E] = \frac{m_{\rm e} v_{\rm th,e} \omega_{\rm p,e}}{e} \qquad [B] = \frac{m_{\rm e}\omega_{\rm p,e}}{e} \tag{3}$$

III. WARM MAGNETIZED PLASMA WITH UNIFORM DENSITY

In order to benchmark the new grid-free model, we first perform simulations of a textbook plasma system that can be treated analytically. We choose a warm homogeneous plasma permeated by a constant background magnetic field oriented along the z-axis. The boundary conditions are periodic in the x and y directions and it is assumed that all derivatives along the z-axis vanish.

We initialize a warm magnetized electron/ion plasma with homogeneous density in a square region of size $L_x = L_y = 100\, r_{\rm L,i}$ containing $N_e = N_i = 10^7$ particles. The normalized plasma parameters are as follows: background magnetic field strength $B_0 = 2$, mass ratio $\mu = 16$ and temperature ratio $\tau = 1$. We integrate the plasma particle trajectories starting at $\omega_{\rm c,i}t = 0$ and ending at $\omega_{\rm c,i}t = 60$ using a time-step of $\omega_{\rm c,i}\Delta t = 0.0067$.

Although particle trajectories are computed by the tree code algorithm entirely without use of a computational grid, the electric potential and electric field are additionally computed on a grid of $N_x \times N_y = 1000 \times 1000$ grid points spanning the simulation domain every 10 timesteps and written to disk. From this data we directly compute the dispersion relation of the warm magnetized plasma by averaging the data along one spatial axis while applying a Fourier transformation (which assumes equidistant sample points) along the other to obtain a spectrum in wave number space at every time step. Following Welch's method[26], we then apply a Parzen windowing function[27] to the resulting time series to obtain a double Fourier spectrum in frequency/wave number space.

FIG. 1 shows the resulting spectrum for a large range of frequencies and wave numbers. It reproduces a multitude of ion cyclotron modes (horizontal lines separated by $\omega_{\rm c,i}$) and also the first three electron modes (horizontal lines at multiples of 16 $\omega_{\rm c,i} = \omega_{\rm c,e}$). It is worth noting that for this particular data sample, the frequency resolution was limited to $\Delta\omega \simeq 0.1\ \omega_{\rm c,i}$ whereas $\omega_{\rm max} \simeq 47\ \omega_{\rm c,i}$. Likewise, the equivalent parameters for the spatial spec-

ACCEPTED MANUSCRIPT

This manuscript was accepted by Phys. Plasmas. Click here to see the version of record.

ACCEPTED MANUSCRIPT

tra were $\Delta k r_{\mathrm{L,i}} \simeq 0.06$, $k_{\max} r_{\mathrm{L,i}} \simeq 31$, whereby the latter could easily be increased by using more diagnostic grid points *independently* of the trajectory calculation. The effective spatial resolution achieved by the tree code is governed by an additional smoothing parameter in eq (1), which in this case was set to $\epsilon \simeq 0.16\, r_{\mathrm{L,i}}$, or more than five times the average interparticle spacing to ensure that the plasma remained effectively collisionless[28].

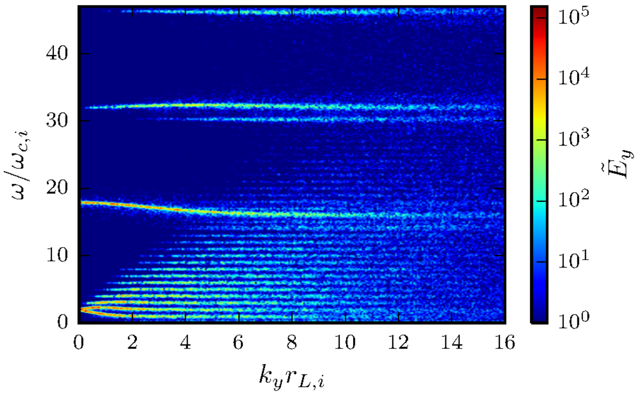

FIG. 1. Frequency/wave number spectrum determined from E_y.

FIG. 2 shows a zoom of the same data over a reduced frequency/wave number range. Overlayed as red dots is the numerical solution of the analytic dispersion relation of the set-up, given in[29]. The energy contained in the electric field in the simulations is concentrated near the modes predicted by the analytic dispersion relation. The agreement between the tree code and the analytic solutions of the long-wavelength ion modes is striking and validates its use as an alternative to PIC for kinetic simulation of magnetized plasmas.

For comparison to the grid-free code results we performed 2D electrostatic PIC simulations with a standard finite-sized model[30] using similar parameters (system size, particle number, mass and temperature ratio, etc.) as described above with quadratic interpolation for particle density and force calculations. Finite-particle size shape factor values of $a_x = \Delta = a_y$, where $\Delta = \lambda_{\mathrm{D,e}}$, were chosen. The spectral analysis of the electric field data was performed using the same procedure as the grid-free model and is shown in FIG. 2 (b).

IV. CLASSICAL KELVIN-HELMHOLTZ SCENARIO

To make a connection with previous kinetic studies of the Kelvin-Helmholtz instability, we now turn our focus to the classical scenario of two counter-streaming plasma-filled half spaces.

We reproduce experiment I from[15] by initializing a warm magnetized plasma in a box of dimensions $L_x = 25.6 r_{\mathrm{L,i}}$ and $L_y = 102.4 r_{\mathrm{L,i}}$ with a mass ratio of $\mu = 16$ and subject to a static magnetic field along the z-axis of strength $B_0 = 2$. Ions are loaded with uniform density, while electrons are loaded at the same density but with a slight perturbation along the x-axis superimposed such that the charge density of the bump satisfies: $\tilde{\rho} = \epsilon_0 \partial_x \tilde{E}$ and $\tilde{E} = -V_0 B_0 \tanh(x/a)$ where V_0 is the velocity shear strength and a is the shear layer width. In this example we take $a = r_{\mathrm{L,i}}$ and $V_0 = \omega_{\mathrm{c,i}} a$. We use a particle loading technique similar to that described in[16] to initialize electrons and ions.

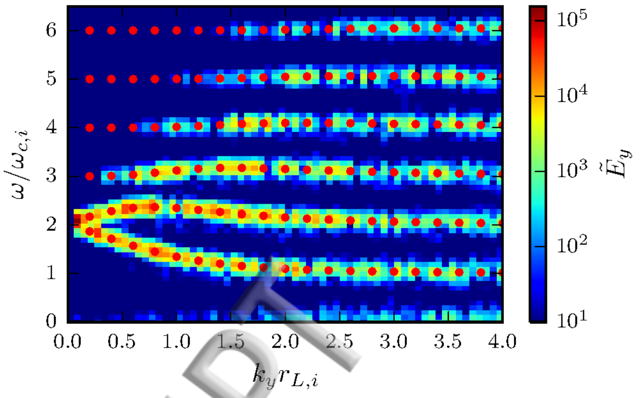

(a) Zoom of the frequency/wave number spectrum in FIG. 1 determined from E_y. The analytic dispersion relation from[29] is denoted by the red dots.

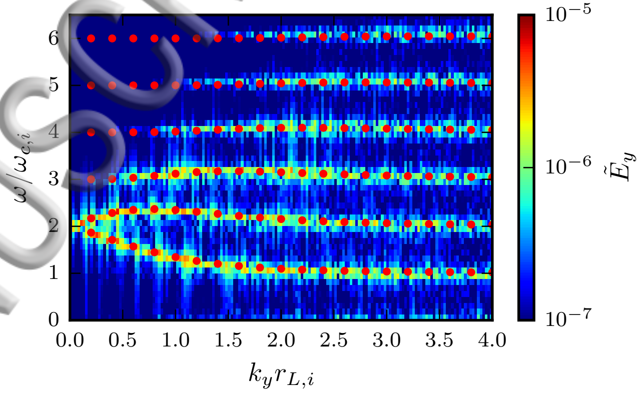

(b) Same analysis as in a) computed instead from a 2D PIC code with 1000×1000 grid points and 10^7 particles per species.

FIG. 2. Details of the dispersion relation determined from the tree algorithm simulations in comparison to the analytical results and results obtained by a PIC simulation.

The boundary conditions for the particle trajectories are periodic in the y-direction. Particles that leave the simulation box at the top are reintroduced at the bottom with their velocities left unchanged. In the x-direction, we apply a reflecting boundary with a suitable particle loading mechanism that follows method II in[31] in order to restrict the particles to the original plasma filled region while suppressing surface currents. For the electrostatic potential and accompanying electric field, the boundary conditions are also periodic in the y-direction and open on both sides in the x-direction.

This manuscript was accepted by Phys. Plasmas. Click here to see the version of record.

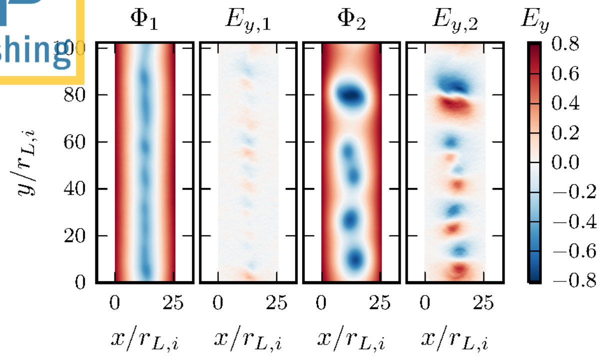

FIG. 3. Electrostatic potential Φ and y-component of electrostatic field E_y. Numerical indices refer to points in time during the linear phase at $\omega_{\mathrm{c,i}}t = 18.75$ (1) and the non-linear phase $\omega_{\mathrm{c,i}}t = 43.75$ (2).

In order to study the dispersion relation of the classical setup, we apply the same Fourier analysis technique as described in section III to the early part of the simulation, up to the point where the instability growth saturates and starts to exhibit non-linear behavior ($\omega_{\mathrm{c,i}}t \simeq 20$), see FIG. 3. We note in passing that the nonlinear phase is also characterized by vortex pairing and merging seen in the Φ_2 plot in FIG. 3, as noted in earlier works[12,14,15,17].

FIG. 4 (a) shows the experimental dispersion relation for the linear phase of the classical setup. Apparently, most of the energy is contained in the purely growing modes at low frequencies and low wave numbers $k_y r_{\mathrm{L,i}} \leq 2$. As in the homogeneous density setup, the first electron modes at $\omega = 16\ \omega_{\mathrm{c,i}}$ are visible. Due to the limited amount of time it takes for the instability to reach the non-linear phase, the frequency resolution is too coarse to distinguish single ion cyclotron modes in this case.

FIG. 4 (b) shows a zoom into the low frequency and low wavenumber part of the dispersion relation. This figure confirms, that most of the energy is contained in the purely growing low frequency modes. A wave number $k_y r_{\mathrm{L,i}} = 0.5$ corresponds to the fastest growing mode with $\lambda_y = 4\pi r_{\mathrm{L,i}}$ in FIG. 3.

To make a quantitative comparison with classical fluid theory and the results in[15], we compute the growth rates of each mode from the development of $E_y(k_y)$ close to the sheath center. We average the $E_y(k_y)$ over a corridor of width 2.56 $r_{\mathrm{L,i}}$ and determine the growth rates $\gamma(k_y)$ by fitting an exponential model $E_y(k_y, t) = E_{y,0}(k_y)\exp(\gamma(k_y)\,t)$. The growth rates are depicted in FIG. 5 together with data from Cai et al.'s PIC-simulations, and once again show excellent agreement.

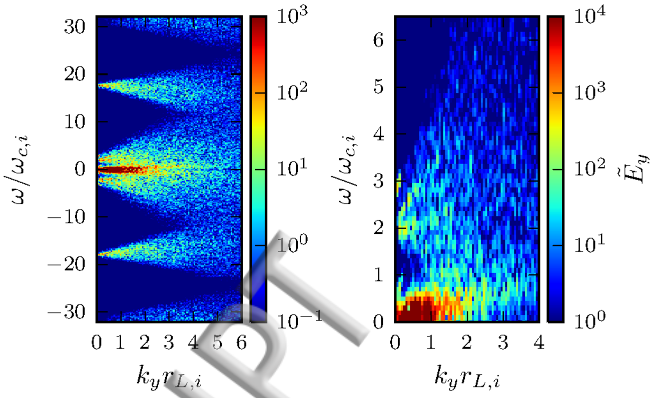

(a) (b)

FIG. 4. Dispersion relation determined from E_y.

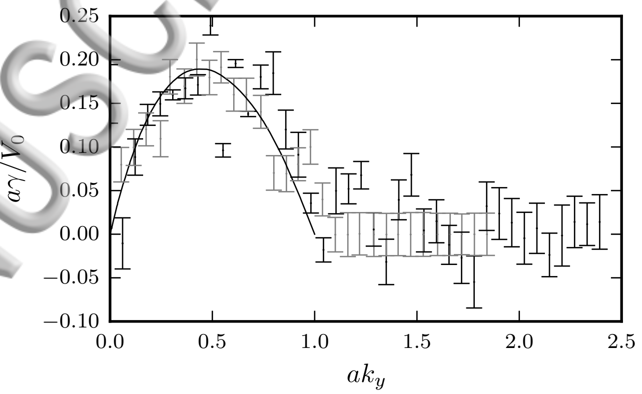

FIG. 5. Normalized growth rate determined from $E_y(k_y)$ at the center of the sheath ($x = 12.5r_{\mathrm{L,i}}$ in FIG. 3). Our results in black, Cai et al. results in grey, theory as solid line.

V. PLASMA-VACUUM INTERFACE

Having established that our numerical model exhibits the expected behavior in the conventional KH case, we now turn to the scenario of primary interest wherein a half-space filled with a plasma at homogeneous density is bounded by another empty half space. The initial dynamics of this situation is quite different to that in the previous section so it is worth illustrating the main features qualitatively before we go into a more detailed analysis.

A. Setup

Initially, the simulation domain is divided into two half-spaces by the y–z-plane. While the half-space along the negative part of the x-axis is empty, the other one is homogeneously filled with a collisionless magnetized two-species plasma. The constant background magnetic field $\boldsymbol{B}_0 = B_0\hat{\boldsymbol{z}}$ is present across the whole region, see FIG. 6 (a).

Under the influence of the magnetic field, some of the particles that are at first close to the plasma-vacuum interface will follow a gyro-motion trajectory that takes

ACCEPTED MANUSCRIPT

This manuscript was accepted by Phys. Plasmas. Click here to see the version of record.

TABLE II. Plasma parameters for the simulation runs of the plasma-vacuum interface instability presented in this paper

Run	$m_\mathrm{i}/m_\mathrm{e}$	$\omega_\mathrm{c,e}/\omega_\mathrm{p,e}$	$\omega_\mathrm{c,i}/\omega_\mathrm{p,i}$	$r_\mathrm{L,i}/\lambda_\mathrm{D,e}$	Box size $L_x \times L_y$ ($r^2_\mathrm{L,i}$)
1	4	2	1	1	50×125
2	16	2	0.5	2	25×62.5
3	100	2	0.2	5	10×25

them out of the plasma half-space. As the Larmor radius is proportional to $\sqrt{mT}$, a heavier ion species at the same temperature as the electrons will be carried farther outside of the boundary, FIG. 6 (b). This creates a positively charged region in front of the bulk plasma while at the same time leaving a surplus of negative charge at its edge, FIG. 6 (c). The resulting electric field is parallel to the density gradient along the x-axis and, in combination with the background magnetic field, creates a sheared drift velocity $v_y(x) = -E_x(x)/B_0$ which feeds the KH instability, FIG. 6 (d).

It is important to note that in contrast to the classical homogeneous setup in Section IV, the resulting shear layer width a in this case results *naturally* from the charge separation driven by the contrasting gyro-motion of the two particle species.

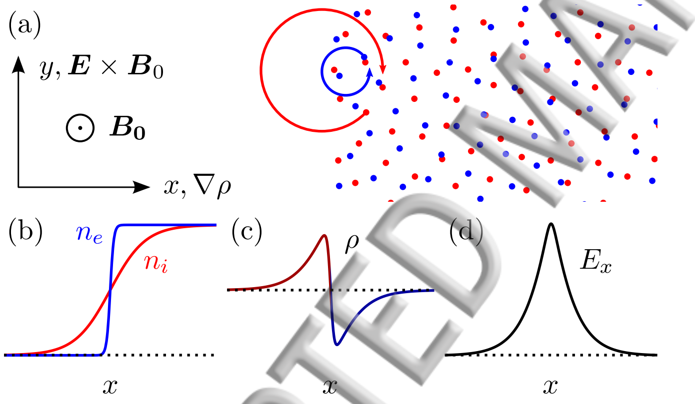

FIG. 6. **(a)** Initial plasma-vacuum interface with orientation of relevant fields and different larmor radii of the two species. **(b)** Different density gradient for the two species. **(c)** Charge separation around the boundary. **(d)** The resulting electric field.

Table I gives the parameters used in our simulations.

B. Eigenmode analysis

Based on the scenario just described, it is possible to derive a simple model of the plasma-vacuum setup from a two fluid picture of the species $\sigma \in \{\mathrm{i}, \mathrm{e}\}$. Initially, the plasma is in a steady state, described by the fluid quantities $n_{\sigma,0} = n_{\sigma,0}(x)$ and $\boldsymbol{v}_{\sigma,0} = v_{\sigma,0}(x)\hat{\boldsymbol{y}}$, the resulting electric field $\boldsymbol{E}_0 = E_0(x)\hat{\boldsymbol{x}}$ and the background magnetic field $\boldsymbol{B}_0 = B_0\hat{\boldsymbol{z}}$.

Assuming perturbations of the form $\Psi(x,y,t) = \bar{\Psi}(x)\exp i(ky-\omega t)$, $\Psi \in \{n_{\sigma,1}, \boldsymbol{v}_{\sigma,1}, \boldsymbol{E}_1\}$ the linearized continuity equation reads

$$i\left(\omega - kv_{\sigma,0}\right)n_{\sigma,1} = ikn_{\sigma,0}v_{\sigma,1,y} + \partial_x(v_{\sigma,1,x}n_{\sigma,0}) \tag{4}$$

The perturbed velocities $\boldsymbol{v}_{\sigma,1}$ are assumed to be due to an $\boldsymbol{E}\times\boldsymbol{B}$ drift caused by the perturbed electric field:

$$v_{\sigma,1,x} = E_{1,y}/B_0 \quad \text{and} \quad v_{\sigma,1,y} = -E_{1,x}/B_0. \tag{5}$$

Finally, Gauss's law and Faraday's law of induction relate the components of the perturbed electric field $\boldsymbol{E}_1$ to one another and to the perturbed charge density $\rho_1 = \sum_\sigma q_\sigma n_{\sigma,1}$:

$$\partial_x E_{1,y} = ikE_{1,x}, \tag{6}$$

$$\partial_x E_{1,x} + ikE_{1,y} = \sum_\sigma q_\sigma n_{\sigma,1}. \tag{7}$$

Combining equations (4), (5), (6), and (7) leads to an eigenvalue equation that takes into account distinct, spatially varying equilibrium density and velocity profiles for each of the two plasma species.

$$\partial_{xx}E_{1,y} = \left(k^2 - \sum_\sigma \frac{kq_\sigma\partial_x n_{\sigma,0}}{B_0(kv_{\sigma,0}-\omega)}\right)E_{1,y} \tag{8}$$

Under the assumption that the equilibrium velocity profiles are equal for both species and based on an $\boldsymbol{E}\times\boldsymbol{B}$ drift due to the equilibrium electric field

$$v_{\sigma,0} = v_0 = -\frac{E_0}{B_0}, \tag{9}$$

$$\partial_x v_0 = -\frac{\partial_x E_0}{B_0} = -\frac{1}{B_0}\sum_\sigma q_\sigma n_{\sigma,0}, \tag{10}$$

the eigenvalue equation given by Cai et al. in[15] can be recovered:

$$\partial_{xx}E_{1,y} = \left(k^2 - \frac{k}{\omega - kv_0}\partial_{xx}v_0\right)E_{1,y}. \tag{11}$$

C. Numerical results and analysis

We now turn to the fully kinetic model of the various plasma-vacuum scenarios given in table II. At the beginning of the simulation, the particles – due to their thermal motion under the influence of the magnetic field

ACCEPTED MANUSCRIPT

This manuscript was accepted by Phys. Plasmas. Click here to see the version of record.

ACCEPTED MANUSCRIPT

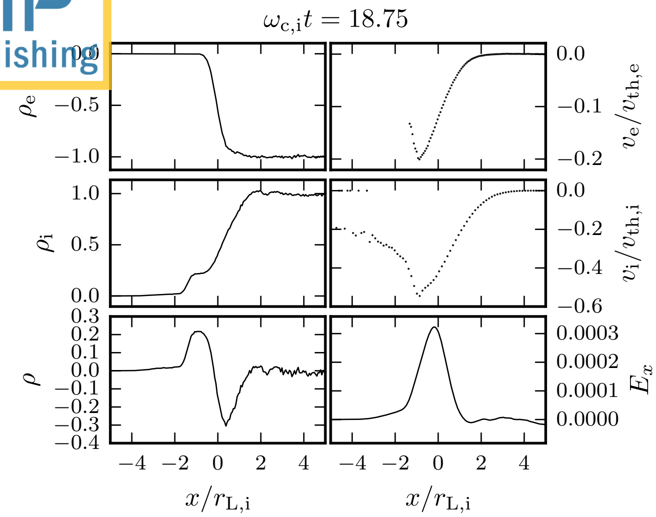

FIG. 7. Per-species charge densities (ρ_{e} and ρ_{i}) and velocities (v_{e} and vi), total charge density (ρ) and x-component of the electric field (E_x) all averaged along the y-axis as functions of x for run 2.

– travel along a circular path that takes those particles with a guiding center close to the initially sharp plasma-vacuum interface outside of the bulk plasma region. As expected the heavier ions have a larger Larmor radius and thus travel farther from the initial interface and already after a time $\omega_{\mathrm{c,i}}t = 18.75$ a charge separation and resulting electric field as shown in FIG. 7 has developed. This electric field in combination with the static background magnetic field causes an $\boldsymbol{E}\times\boldsymbol{B}$ drift of the guiding centers in the negative y-direction as illustrated schematically in FIG. 6.

After a few ion cyclotron periods, a periodic deformation of the initially straight plasma-vacuum interface grows along the y-axis in the densities of both species, causing in turn a periodic perturbation of the y-component of the electric field. FIG. 8 shows the per-species charge densities as well as the electric potential and y-component of the electric field during the linear phase of the instability ($\omega_{\mathrm{c,i}}t = 18.75$) and later at the onset of the non-linear phase ($\omega_{\mathrm{c,i}}t = 31.25$).

1. Tracer particle trajectories

As the velocity shear in the plasma-vacuum interface scenario is not externally imposed but rather develops as a result of the initial conditions, we use the trajectories of tracer particles to determine the characteristic scales of the shear layer, namely its width a and the shear strength V_0. We initialize a large number of ions close to the plasma vacuum boundary with initial conditions (particle positions and velocity distribution) that are compatible to those used in the simulations. The particle trajectories are integrated off-line, i.e., we re-use the time-dependent electric field data that has been written to disk during the simulations to solve the ion equation of motion

$$\ddot{\boldsymbol{x}} = \frac{q_i}{m_i}\left(\dot{\boldsymbol{x}} \times \boldsymbol{B}_0 + \boldsymbol{E}_0\right). \tag{12}$$

For simplicity, internal forces between these sample ions are not taken into account.

FIG. 9 shows example tracer particle trajectories. The trajectory in the leftmost panel is typical for a particle close to the plasma boundary with a small drift velocity. Due to a high initial (thermal) velocity, the particle is able to overcome the spatially limited electric field and hence only a part of its overall trajectory is influenced by it. Conversely, the trajectory shown in the middle panel is typical for a large drift velocity. It belongs to a particle with a comparatively low initial velocity which is almost completely deflected by the electric field at the boundary and follows a severely deformed trajectory. The rightmost panel shows the trajectory of an ion with a guiding center inside the bulk plasma, far away from the bound-

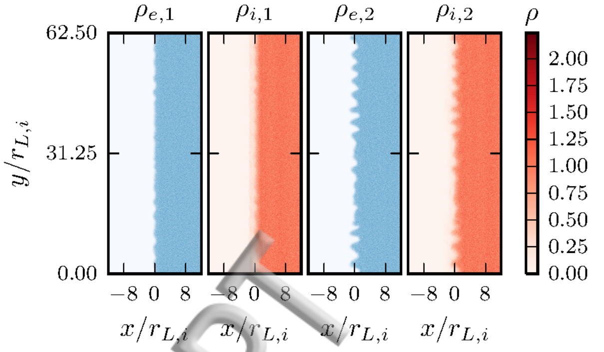

(a) Per-species charge densities

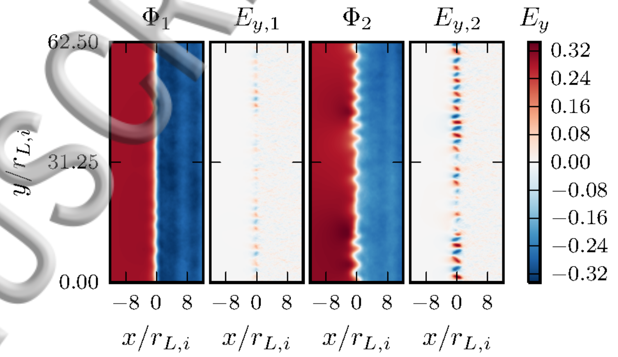

(b) Electrostatic potential and field

FIG. 8. Per-species charge densities ρ_e and ρ_i and electrostatic potential Φ and y-component of the electrostatic field E_y (units as in equation (3)) for run 2. Numerical indices refer to points in time during the linear phase at $\omega_{\mathrm{c,i}}t = 18.75$ (1) and the non-linear phase $\omega_{\mathrm{c,i}}t = 31.25$ (2).

This manuscript was accepted by Phys. Plasmas. Click here to see the version of record.

ary that is not under the influence of an electric field and therefore does not drift.

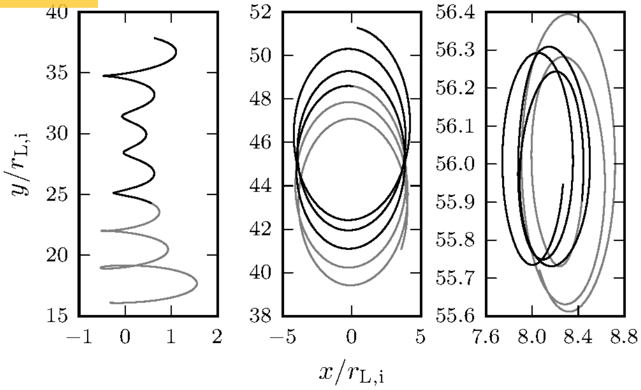

FIG. 9. Example ion trajectories in black (grey) starting at $\omega_{\mathrm{c,i}}t = 0$ and ending at $\omega_{\mathrm{c,i}}t = 18.75$ ($\omega_{\mathrm{c,i}}t = 31.25$) for run 2. Shown are the particles with a small (left) and a large (middle) drift velocity at the plasma edge as well as a randomly selected particle (left) inside the bulk plasma.

We calculate the drift velocity v_{drift} for every particle by taking the displacement of the guiding center along the y-axis during a certain time interval and dividing by the length of that interval. To determine the shape of the velocity shear profile, we calculate $\langle v_{\mathrm{drift}}(x)\rangle$ by partitioning the particle population into slices based on the x-coordinate of their guiding centers and taking the mean drift velocity of each slice. The resulting profile is shown in 7. Finally, we use a fit of a hyperbolic tangent profile $\langle v_{\mathrm{drift}}(x)\rangle = V_0\left(\tanh\left(\frac{x-x_0}{a}\right) - 1\right)$ to determine a and V_0.

Figure 10 shows the local velocity distribution for three of the slices placed outside the bulk plasma region, close to the plasma-vacuum boundary and inside the bulk plasma. While the distribution is centered around zero and narrowly peaked inside the bulk plasma, its center moves towards larger absolute values moving across the boundary, outside of the plasma. At the same time, the width of the distribution increases and the total number of particles in a slice becomes less.

2. Growth rates

The dispersion curve of the instability during the linear phase is determined by applying the same procedure described in section IV. To obtain a representative sample of the field in the edge region, several $E_y(k_y)$ spectra were averaged across a layer that is centered on the plasma-vacuum interface and 5 $r_{\mathrm{L,i}}$ wide (see FIG. 7). FIG. 11 shows two comparisons of the growth rate spectra for runs 1 – 3 with different kinds of normalization applied.

First, FIG. 11 (a) shows the wave numbers and associated growth rates in terms of the electron Debye length

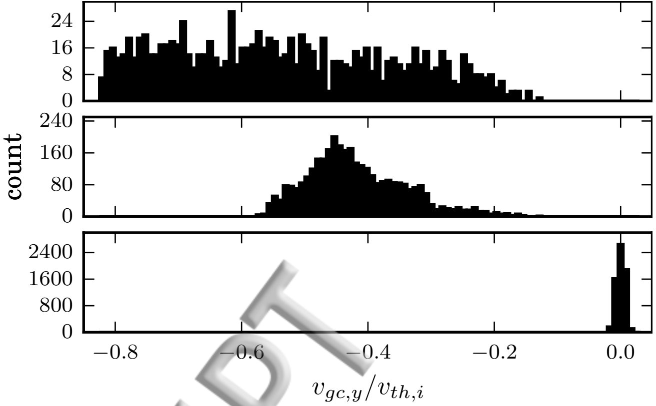

FIG. 10. Slices of the spatially resolved velocity distribution $f(x_{gc}, v_{gc,y})$ at $x \simeq -r_{\mathrm{L,i}}$ (top) $x \simeq 0$ (middle) and $x \simeq 6r_{\mathrm{L,i}}$ (bottom) for run 2

and electron plasma frequency, which are the same for all three runs. In this set of units, all three runs exhibit comparable growth rates at comparable wavelengths. The analytic model for the classical Kelvin-Helmholtz instability however predicts a scaling of the wave numbers of unstable modes with the inverse of the shear layer width a and of the growth rates themselves with the ratio of shear strength to layer width V_0/a. As noted earlier, the shear layer and its characteristic quantities a and V_0 are not externally imposed as they are in the classical setup, but develop self-consistently during the course of the simulation. Their values, as determined from the particle trajectories (see section V C 1), are given in table III. The variation between runs, especially in the shear strength V_0, in contrast to the very similar growth rates in all three runs suggests that the ion velocity shear cannot be the only driving mechanism behind the instability.

Second, FIG. 11 (b) shows the three spectra normalized by respective effective shear layer widths $\tilde{a}$ and velocity shear strengths $\tilde{V}_0$. These effective normalization factors where determined by performing a least squares fit of the analytic growth rate spectrum for the classical Kelvin-Helmholtz instability to the experimental growth rate spectra. The effective parameters can be understood as the characteristic scales that the ion velocity shear layers would need to exhibit in order to be explained by the theory for the classical Kelvin-Helmholtz scenario. The resulting $\tilde{a}$ and $\tilde{V}_0$ for all runs can also be found in table III. Comparing them to the actual scales of the ion velocity shear layers (a and V_0) found by means of the particle trajectories, explaining the growth rate spectra by means of the analytical model for the classical scenario would indicate a more narrow layer at significantly reduced shear strength in every run.

ACCEPTED MANUSCRIPT

This manuscript was accepted by Phys. Plasmas. Click here to see the version of record.

TABLE III. Effective shear layer width $\tilde{a}$ and effective velocity shear strength $\tilde{V}_0$

Run	$a/r_{\mathrm{L,i}}$	$V_0/v_{\mathrm{th,i}}$	$\tilde{a}/r_{\mathrm{L,i}}$	$\tilde{V}_0/v_{\mathrm{th,i}}$
1	0.70	0.10	0.36	0.051
2	0.75	0.29	0.18	0.10
3	0.63	0.86	0.072	0.26

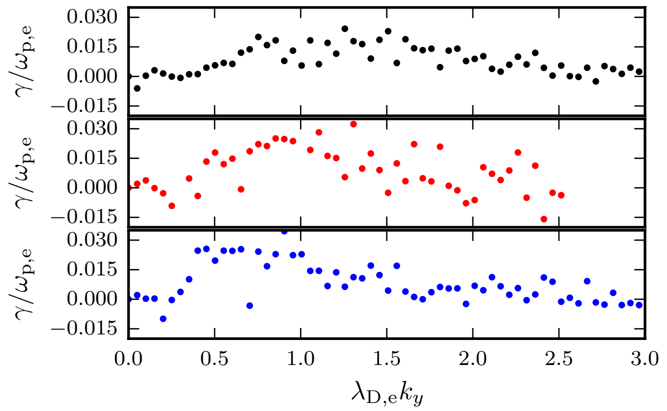

(a) Spectra with no normalization applied, runs 1 – 3 are displayed in order from top to bottom

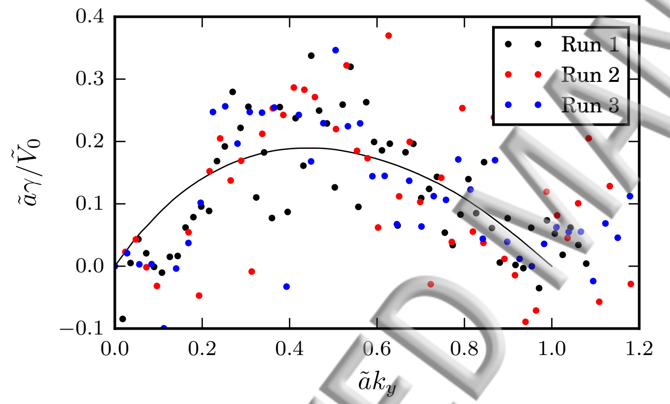

(b) Spectra normalized according to effective shear layer width $\tilde{a}$ and effective velocity shear strength $\tilde{V}_0$, see table III

FIG. 11. Comparison of growth rate spectra from runs 1 – 3

3. Dispersion relation

FIG. 12 shows the dispersion relation of the instability in the plasma-vacuum set-up. Similar to the dispersion relation of the classical case, most of the power is concentrated around lower frequencies and wave numbers corresponding to the growing unstable modes. Some of the lowest ion cyclotron modes (divided by $\omega_{\mathrm{c,i}}$) are also visible as is the lowest electron mode (at $\omega = 16\,\omega_{\mathrm{c,i}}$).

The modes show a noticeable slant towards higher frequencies at higher wave numbers. This slope is roughly compatible with $\omega = V_0 k_y$. The slant due to the shear velocity V_0 is superimposed in the upper panel of FIG. 12 while the lower part displays additional curves due to the minimum and the maximum velocities. Compared to the equivalent dispersion plot in FIG. 4 (a) for the classical KH case, we can see that apart from the shift in spectral density to higher mode numbers, the net drift ensures that the unstable modes also connect along the surface, leading to more rapid mixing during the linear growth phase.

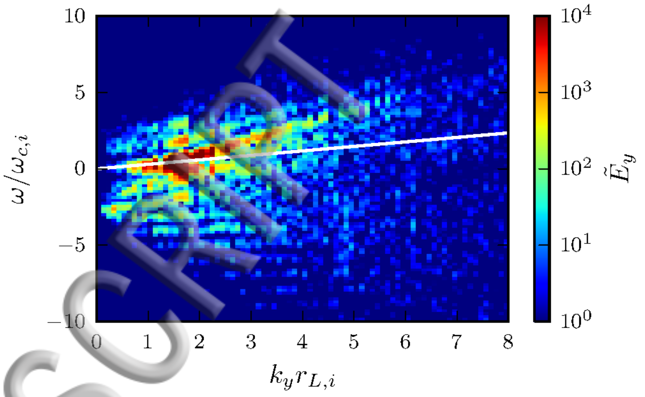

FIG. 12. Dispersion relation determined from E_y for run 2. The velocity shear strength V_0 is shown for reference.

VI. CONCLUSIONS

In the present work we have revisited a commonly recurring problem in plasma boundary layers – the Kelvin Helmholtz instability – with a particular emphasis on the high-frequency kinetic regime likely to be prevalent in plasma-vacuum interfaces found in plasma devices and certain astrophysical contexts. In doing so we have introduced and a new mesh-free kinetic model, establishing its validity via standard benchmarks for magnetized plasmas. In the simplest scenario, the dispersion relation of a homogeneous, magnetized plasma was obtained and verified with high spectral resolution, the results with the new model comparing favorably with equivalent calculations using a standard 2-dimensional PIC code.

Previous kinetic simulations of the classical Kelvin-Helmholtz instability generated by a shear flow in a homogeneous plasma could also be reproduced by the new model, the numerical results for the instability growth curve $\gamma(k)$ also agreeing well with fluid theory. This benchmarked model was then used to tackle the more typical plasma-vacuum scenario in which an $\boldsymbol{E}\times\boldsymbol{B}$ drift is set up via the reversed sheath created by the ion Larmor orbits. Despite the topological differences to the classical KH case – in particular the fact that the electron and ion density profiles of the plasma-vacuum interface were allowed to evolve self-consistently – the latter nevertheless exhibits a KH-like instability with a similar characteristic growth curve. More detailed analysis of the ion orbits reveals that a self-similar growth curve for different mass ratios (analogous to the classical case) by rescaling the

ACCEPTED MANUSCRIPT

This manuscript was accepted by Phys. Plasmas. Click here to see the version of record.

AIP Publishing

shear flow velocities and layer width to values reflecting the reduced population of boundary layer ions actually driving the instability.

In absolute terms, the PV incarnation of the KH instability grows more slowly than its classical counterpart, but we still observe the onset of the nonlinear phase after a few tens of ion cyclotron periods, acting on a scale of several ion Larmor radii. From FIG. 11 (a) and FIG. 12 the real frequency and growth rates can be estimated and compared to observed density gradient-driven/KH fluctuations using LAPD parameters[8,32]. With maximum growth rate $\gamma/\Omega_{c,i} \simeq 0.00375$ from FIG. 11 (a) and $f_{c,i} \simeq 450kHz$ in LAPD, the growth time is approximately $94.3\mu sec$. FIG. 12 indicates a broad frequency range above and below the ion cyclotron frequency with perpendicular wavelength range $k_y r_{L,i} \sim 0.5{-}5$ dominating. This indicates that kinetic effects may well be important for KH-induced instabilities in linear plasma devices such as the LAPD and PSI-2. Inspection of longer runs with our model reveals nonlinear edge turbulence similar to that observed with fluid simulations in[33] performed with parameters close to the LAPD plasma. While analysis of the nonlinear regime in cylindrical geometry is beyond the scope of this work, the present work indicates that fully kinetic simulations of this scenario to determine the cross-field particle and heat transport are well within reach using present-day supercomputers.

ACKNOWLEDGMENTS

Funding for this work was provided in part by the Helmholtz International Research Group 0048. Computing time on the systems at Jülich Supercomputing Centre was provided by the JARA HPC project JZAM04. The work of RDS is supported by the Natural Sciences and Engineering Research Council (NSERC) of Canada.

[1] W. I. Axford, Planetary and Space Science **12**, 45 (1964).
[2] D. J. Southwood, in *Proc. Chapman Conf. on Magnetospheric Boundary Layers*, Vol. 148, edited by B. Battrick, Eur. Space Agency (Spec. Publ. ESA SP, 1979) p. 357.
[3] M. M. Cowee, D. Winske, and S. P. Gary, J. Geophys. Res. **115**, A06214 (2010).
[4] D. L. Jassby, Physics of Fluids **15**, 1590 (1972).
[5] T. Huld, S. Iizuka, H. L. Pécseli, and J. J. Rasmussen, Plasma Physics and Controlled Fusion **30**, 1297 (1988).
[6] T. Huld, a. H. Nielsen, H. L. Pecseli, and J. Juul Rasmussen, Physics of Fluids B: Plasma Physics **3**, 1609 (1991).
[7] F. Brochard, E. Gravier, and G. Bonhomme, Physics of Plasmas **12**, 062104 (2005).
[8] S. Zhou, W. Heidbrink, H. Boehmre, R. McWilliams, T. Carter, S. Vincena, B. Friedman, and D. Schaffner, Physics of Plasmas **19** (2012), 10.1063/1.3677361.
[9] S. Chandrasekhar, *Hydrodynamic and Hydromagnetic Stability* (Oxford University Press, 1961).
[10] A. Miura, Phys. Rev. Lett. **49**, 779 (1982).
[11] P. L. Pritchett and F. V. Coroniti, J. Geophys. Res. **89**, 168 (1984).
[12] P. L. Pritchett, Phys. Fluids **30**, 272 (1987).
[13] G. Ganguli, Y. C. Lee, and P. Palmadesso, Phys. Fluids **28**, 761 (1985).
[14] W. Horton and T. Tajima, Phys. Fluids **30**, 3485 (1987).
[15] D. Cai, L. R. O. Storey, and T. Itoh, Phys. Fluids B **5**, 3507 (1993).
[16] D. Cai, L. R. O. Storey, and T. Neubert, J. Comp. Phys. **107**, 84 (1993).
[17] K. Theilhaber and C. K. Birdsall, Phys. Rev. Lett. **62**, 772 (1989).
[18] K. Theilhaber and C. K. Birdsall, Phys. Fluids B **1**, 2244 (1989).
[19] K. Theilhaber and C. K. Birdsall, Phys. Fluids B **1**, 2260 (1989).
[20] T. Umeda, J.-i. Miwa, Y. Matsumoto, T. K. M. Nakamura, K. Togano, K. Fukazawa, and I. Shinohara, Phys. Plasmas **17** (2010), 10.1063/1.3422547.
[21] J. Barnes and P. Hut, Nature **324**, 446 (1986).
[22] K. Kudin and G. Scuseria, Chemical Physics Letters **283**, 61 (1998).
[23] M. Winkel, *High-resolution Simulations of Strongly Coupled Coulomb Systems with a Parallel Tree Code*, Ph.D. thesis, RWTH Aachen (2013).
[24] P. Gibbon, F. N. Beg, E. L. Clark, R. G. Evans, and M. Zepf, Physics of Plasmas **11**, 4032 (2004).
[25] M. Winkel, R. Speck, H. Hübner, L. Arnold, R. Krause, and P. Gibbon, Computer Physics Communications **183**, 880 (2012).
[26] P. Welch, IEEE Transactions on Audio and Electroacoustics **15**, 70 (1967).
[27] F. Harris, Proceedings of the IEEE **66**, 51 (1978).
[28] P. Gibbon, Physical Review E **72**, 026411 (2005).
[29] I. B. Bernstein, Physical Review **109**, 10 (1958).
[30] J. M. Dawson, Reviews of Modern Physics **55**, 403 (1983).
[31] H. Naitou, S. Tokuda, and T. Kamimura, Journal of Computational Physics **33**, 86 (1979).
[32] J. C. Perez, W. Horton, R. D. Bengtson, and T. Carter, Physics of Plasmas **13**, 055701 (2006).
[33] B. N. Rogers and P. Ricci, Physical Review Letters **104**, 225002 (2010).

ACCEPTED MANUSCRIPT

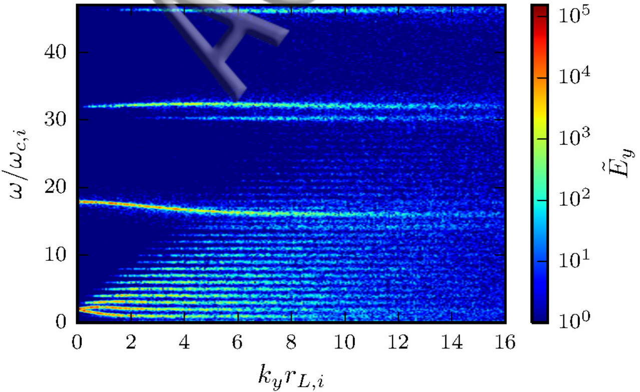
40
30
20
10
0
$\omega/\omega_{c,i}$
0
2
4
6
8
10
12
14
16
$k_y r_{L,i}$
10^5
10^4
10^3
10^2
10^1
10^0
$\tilde{E}_y$

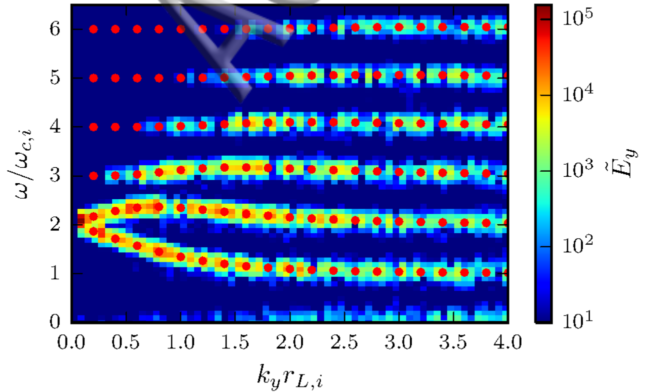
$\omega/\omega_{c,i}$
0
1
2
3
4
5
6
0.0
0.5
1.0
1.5
2.0
2.5
3.0
3.5
4.0
$k_y r_{L,i}$
10^1
10^2
10^3
10^4
10^5
$\tilde{E}_y$

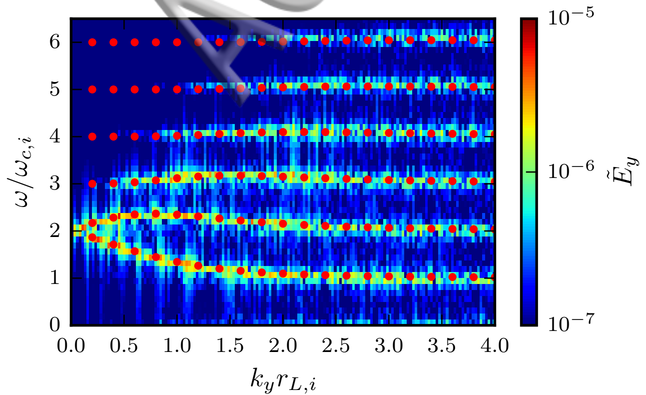
$\omega/\omega_{c,i}$
0
1
2
3
4
5
6
0.0
0.5
1.0
1.5
2.0
2.5
3.0
3.5
4.0
$k_y r_{L,i}$
10^{-5}
10^{-6}
10^{-7}
$\tilde{E}_y$

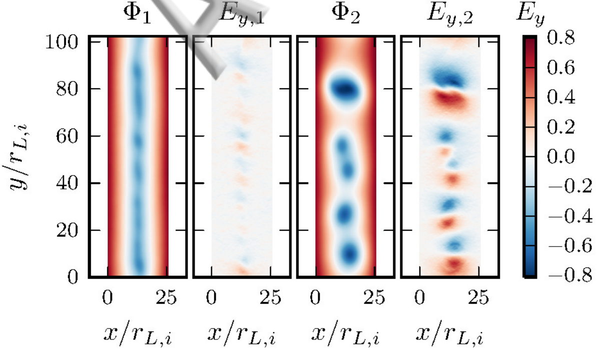
Φ_1
$E_{y,1}$
Φ_2
$E_{y,2}$
E_y
$y/r_{L,i}$
0
20
40
60
80
100
0
25
$x/r_{L,i}$
0.8
0.6
0.4
0.2
0.0
−0.2
−0.4
−0.6
−0.8

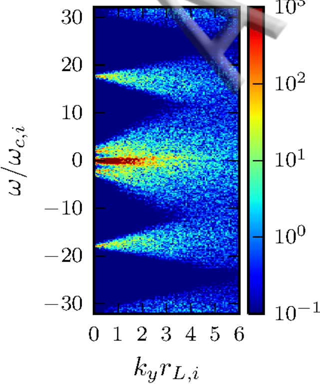
30
20
10
0
−10
−20
−30
$\omega/\omega_{c,i}$
0
1
2
3
4
5
6
$k_y r_{L,i}$
10^3
10^2
10^1
10^0
10^{-1}

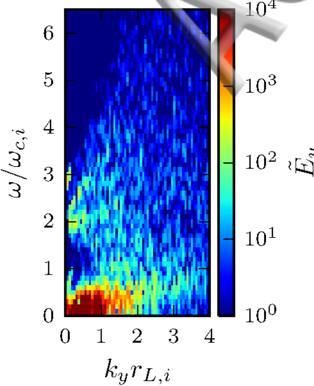
$\omega/\omega_{c,i}$
0
1
2
3
4
5
6
$k_y r_{L,i}$
0
1
2
3
4
$\tilde{E}_y$
10^0
10^1
10^2
10^3
10^4

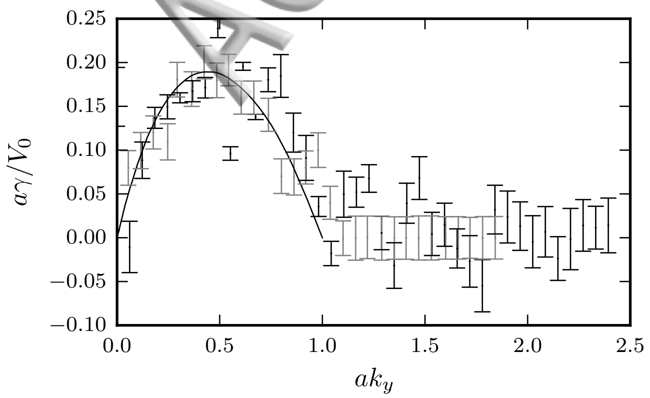
0.25
0.20
0.15
0.10
0.05
0.00
−0.05
−0.10
$a\gamma/V_0$
0.0
0.5
1.0
1.5
2.0
2.5
ak_y

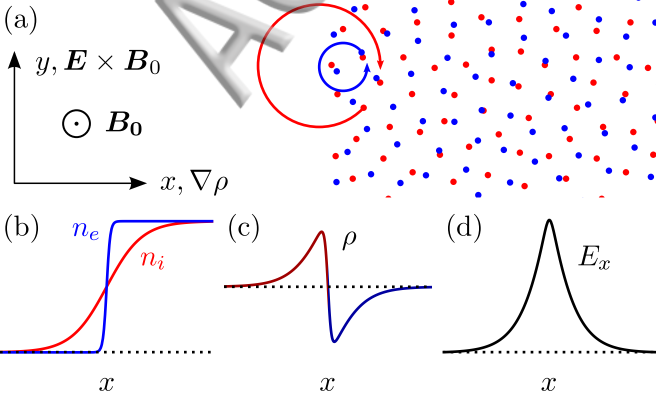
(a)
$y, \boldsymbol{E} \times \boldsymbol{B}_0$
$\odot\ \boldsymbol{B_0}$
$x, \nabla\rho$
(b)
n_e
n_i
x
(c)
ρ
x
(d)
E_x
x

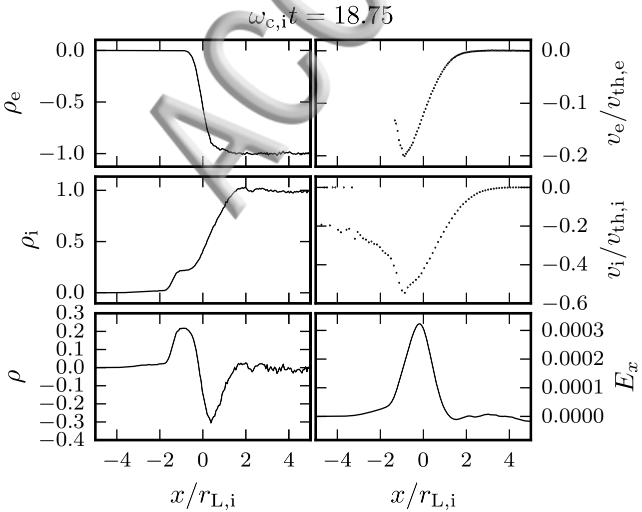
$\omega_{\mathrm{c,i}}t = 18.75$
ρ_{e}
0.0
−0.5
−1.0
$v_{\mathrm{e}}/v_{\mathrm{th,e}}$
0.0
−0.1
−0.2
ρ_{i}
1.0
0.5
0.0
$v_{\mathrm{i}}/v_{\mathrm{th,i}}$
0.0
−0.2
−0.4
−0.6
ρ
0.3
0.2
0.1
0.0
−0.1
−0.2
−0.3
−0.4
E_x
0.0003
0.0002
0.0001
0.0000
−4
−2
0
2
4
$x/r_{\mathrm{L,i}}$
−4
−2
0
2
4
$x/r_{\mathrm{L,i}}$

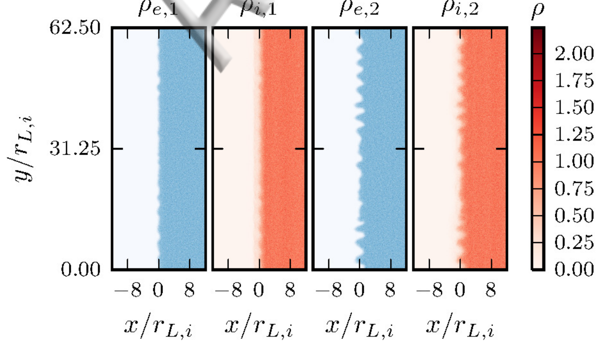

$\rho_{e,1}$
$\rho_{i,1}$
$\rho_{e,2}$
$\rho_{i,2}$
ρ
62.50
31.25
0.00
$y/r_{L,i}$
-8
0
8
$x/r_{L,i}$
2.00
1.75
1.50
1.25
1.00
0.75
0.50
0.25
0.00

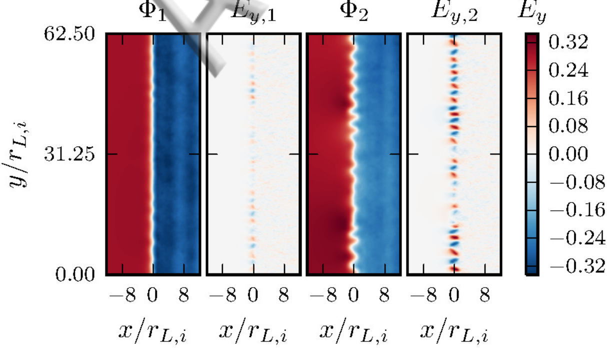
Φ_1
$E_{y,1}$
Φ_2
$E_{y,2}$
E_y
62.50
31.25
0.00
$y/r_{L,i}$
−8 0 8
$x/r_{L,i}$
0.32
0.24
0.16
0.08
0.00
−0.08
−0.16
−0.24
−0.32

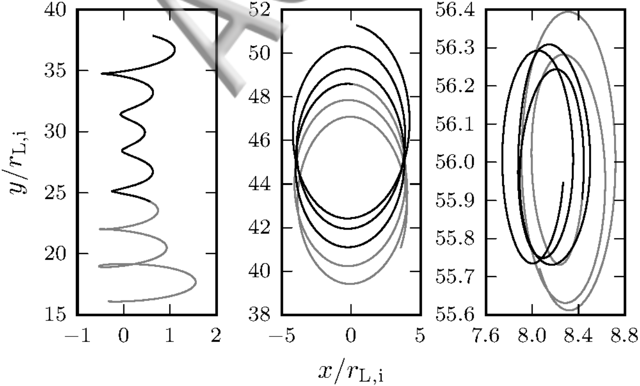

$y/r_{\rm L,i}$
40
35
30
25
20
15
−1
0
1
2
52
50
48
46
44
42
40
38
−5
0
5
56.4
56.3
56.2
56.1
56.0
55.9
55.8
55.7
55.6
7.6
8.0
8.4
8.8
$x/r_{\rm L,i}$

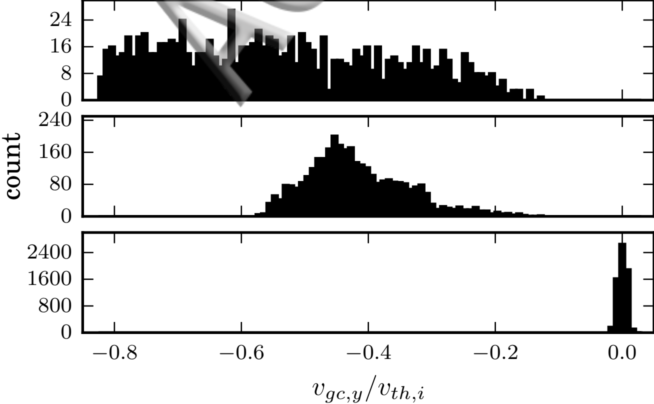
24
16
8
0
240
160
80
0
2400
1600
800
0
count
−0.8
−0.6
−0.4
−0.2
0.0
$v_{gc,y}/v_{th,i}$

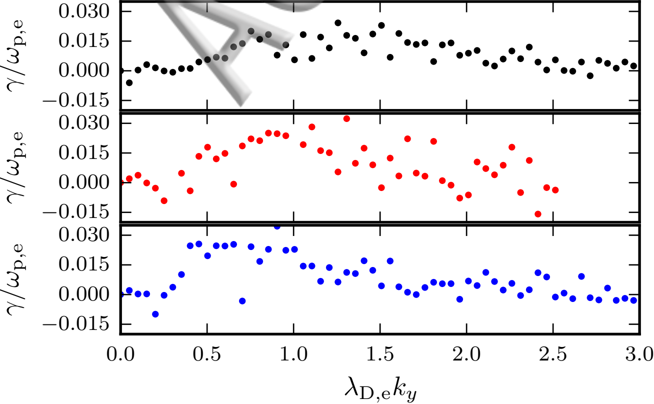
$\gamma/\omega_{\mathrm{p,e}}$
0.030
0.015
0.000
−0.015
$\gamma/\omega_{\mathrm{p,e}}$
0.030
0.015
0.000
−0.015
$\gamma/\omega_{\mathrm{p,e}}$
0.030
0.015
0.000
−0.015
0.0
0.5
1.0
1.5
2.0
2.5
3.0
$\lambda_{\mathrm{D,e}}k_y$

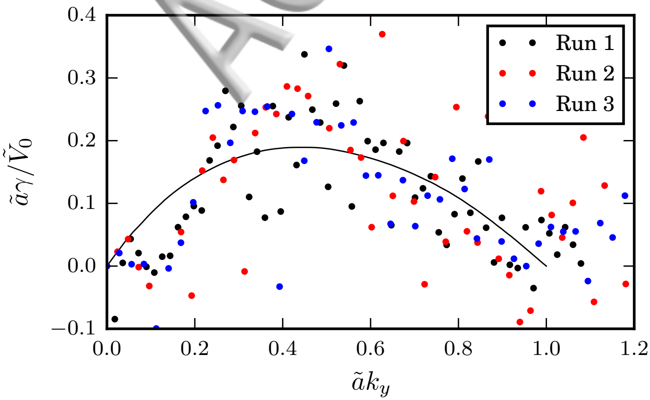
0.4
0.3
0.2
0.1
0.0
−0.1
$\tilde{a}\gamma/\tilde{V}_0$
0.0
0.2
0.4
0.6
0.8
1.0
1.2
$\tilde{a}k_y$
Run 1
Run 2
Run 3

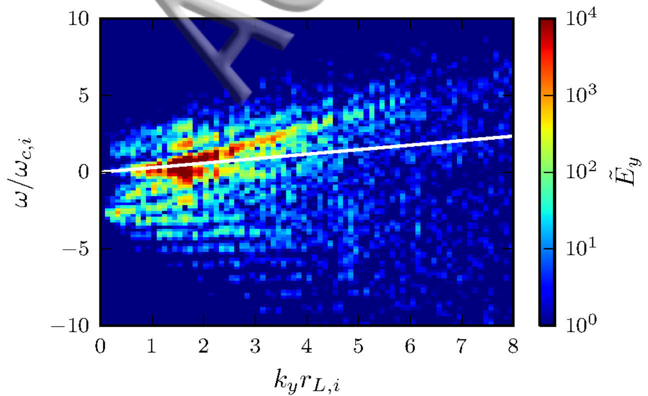

$\omega/\omega_{c,i}$
10
5
0
-5
-10
0
1
2
3
4
5
6
7
8
$k_y r_{L,i}$
10^4
10^3
10^2
10^1
10^0
$\tilde{E}_y$